

Space Radiation Effects Modeling and Analysis of Quantum Dot Based Photovoltaic Cells

Alexander I. Fedoseyev ^{a*}, Marek Turowski ^a, Ashok Raman ^a, Edward W. Taylor ^b, Seth Hubbard ^c,
Stephen Polly ^c, Qinghui Shao ^d and Alexander A. Balandin ^d

^a CFD Research Corporation (CFDRC), 215 Wynn Drive, Huntsville, AL 35805

^b International Photonics Consultants Inc., 38 Knife Edge Place, Pagosa Springs, Colorado, 81147

^c Nanopower Labs, Rochester Institute of Technology, Rochester, NY

^d Nano-Device Laboratory, Department of Electrical Engineering, UC-Riverside, CA 92521

ABSTRACT

For applications in space systems, devices based on novel nanomaterials offer significant advantages over traditional technologies in terms of light-weight and efficiency. Examples of such novel devices include quantum dot (QD) based solar cells and photodetectors. However, the response of these devices to radiation effects is not well understood, and radiation effects modeling tools are not yet available. In this paper we review our numerical models and experimental investigation of radiation effects in quantum dot based solar cells. In the natural, high-radiation environment of space all solar cells suffer from degradation. Although some studies have been conducted, and test data collected, on the performance of solar cells in a radiation environment, the mechanisms of radiation-induced degradation of quantum dot superlattices (QDS) has yet to be established. We have conducted proton irradiation experiments to provide a direct comparison of radiation hardness of quantum dot based cells and regular solar cells. An approach to the development of Nano-scale Technology Computer Aided Design (NanoTCAD) simulation software for simulation of radiation effects in QDS-based photovoltaic (PV) devices is presented. The NanoTCAD tools are based on classical drift-diffusion and quantum-mechanical models for the simulation of QD PV cells.

Keywords: Nanostructures, photovoltaic, radiation effects, quantum dot, nanodevices, NanoTCAD.

1. INTRODUCTION

Solar cells and photodetectors based on quantum dot superlattices (QDS) have the potential to increase the photon conversion efficiency up to about 60% by utilizing the photo-generated hot carriers, which can produce higher voltages and higher photocurrents [1]. Energetic proton-induced radiation damage creates Frenkel pairs wherein atoms are dislodged from a lattice site to an interstitial position, leaving behind a vacancy. The interstitial can migrate until it finds a stable site, such as a surface. This is different from the radiation effects observed in semiconductor submicron devices [2]. Three-dimensional (3D) physical models were developed for radiation-induced lattice defects (traps), featuring: (i) multiple energy levels in semiconductor bandgap, (ii) various, user-defined trap densities for each energy-level (within bandgap), (iii) user-defined capture cross-sections for each trap level. This model has been implemented into CFDRC's 3D device simulator NanoTCAD. The addition of interface and bulk trap models enables simulations of charge trapping and de-trapping in both steady-state and transient analyses. This provides the means for accurate simulations of QDS solar cell performance and their degradation due to effects of space radiation.

Modeling and simulation tools are strongly needed to better understand and predict behavior of nano-devices and novel nano-materials for space applications, assess technologies, devices, and materials for new electronic systems [1, 4, 5]. The QD models are being integrated into our photonic-electronic device simulator NanoTCAD [3, 4], which is intended for the optimization of QD superlattices as well as for the development and exploration of new solar cell designs. A prototype structure for the modeling of the quantum-dot superlattice (QDS)-based photovoltaic (PV) cell is shown in

*Corresponding author; electronic mail: aif@cfdrc.com, phone: (256)726-4928; fax: (256)726-4806; www.cfdrc.com

Fig. 1. The basic element of this PV cell is a stack of quantum dots arrays, referred to as QDS. The QDS can be implemented on Si/Ge or other material systems including III-V group materials such as GaAs. The QDS forms an intrinsic layer in a regular n-i-p (p-i-n) solar cell configuration. Quantum confinement of charge carriers (electrons and holes) in variable-size quantum dots, which form the i-layer, increases the effective band gap of the material. The quantum dot size variation allows one to optimize absorption at different wavelengths and create a multicolor quantum PV cell with estimated efficiency > 50% [1].

2. EFFICIENT APPROACH FOR ACCURATE SOLUTION OF QUANTUM AND DRIFT-DIFFUSION LEVEL MODELS

Drift-diffusion (DD) based models have a long and fruitful history in 3D simulations of not only modern electronic, but also optoelectronic, devices. In recent years, however, a new class of devices has been emerging and they require tools that include quantum effects (quantum well, tunnel junction, QD nanostructures, etc.) but also call for efficient numerical implementation. We have proposed and tested in our NanoTCAD 3D device simulator a number of the reduced models for quantum scale of the problem, which have been successfully verified on experimental and numerical data [3, 6].

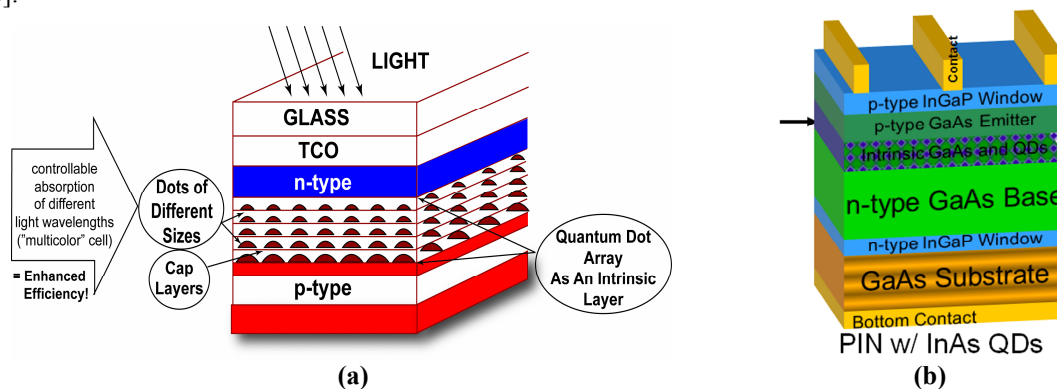


Figure 1. (a) Structure of the PV cell based on the quantum dot superlattice (QDS), which is used as a prototype for the development of the PV cell simulation tools. The structure contains a stack of multiple quantum-dot arrays with variable dot size, which maximizes absorption of the different light wavelengths in a controllable way (resulting in calculated efficiency of more than 50% [1]). Figure (b) shows actual design of QD p-i-n solar cell structure.

The modeling of the photovoltaic cell (see Fig. 1 (a)) is conducted with 3D NanoTCAD device simulator, which uses the quantum level computed transport parameters for the i-layer, the device region containing quantum dot superlattice, while for other device regions, the classical DD models were used. Typical I-V curves for photovoltaic device, silicon p-i-n solar cell, calculated with NanoTCAD are shown in Fig. 2(a), comparison with the experimental data for PV cells developed at RIT are shown in Fig. 2(b). The multiscale photovoltaic (PV) models are being integrated within the advanced software tool NanoTCAD. This integration provides a user-friendly interface and a large database of the semiconductor material properties available in NanoTCAD. It also makes possible a complete PV-cell simulation including both quantum and classical models for the appropriate PV-cell elements, both DC and transient regimes, etc. The models are currently being extended to incorporate simulation of the electron-phonon transport in QDS made of semiconductors with both cubic and hexagonal crystal lattice, e.g., InAs/GaAs, Ge/Si, CdSe, ZnO. The drift-diffusion model implemented in NanoTCAD is described below.

Drift-Diffusion Model Drift-diffusion models are formulated based on continuity equations for electrons and holes and Poisson equation for electrostatic potential. They are able to provide good comparison with experimental data for transistors with channel length down to 15 nm. Conservation of charge for electrons is represented by the continuity equation:

$$q \frac{\partial n}{\partial t} + \nabla \cdot J_n = qR, \quad (1)$$

and similarly for holes as

$$q \frac{\partial p}{\partial t} + \nabla \cdot J_p = -qR, \quad (2)$$

where the electron current is

$$J_n = q\mu_n (U_T \nabla n - n \nabla \Psi) \quad (3)$$

and hole current is

$$J_p = -q\mu_p (U_T \nabla p - p \nabla \Psi). \quad (4)$$

Here n and p are electron and hole densities [$1/\text{cm}^3$], Ψ is electrostatic potential [V], q is carrier charge (electron charge e), $U_T = \frac{k_B}{q}$, and diffusion coefficients are $D_n = U_T \mu_n$ and $D_p = U_T \mu_p$ [cm^2/s].

Electron and hole mobility μ_n, μ_p are calculated parameters (models depend on the material, device, or calculated from quantum or kinetic level problems). Electrostatic potential, which appears in current equations, is governed by Poisson equation

$$\nabla \varepsilon \nabla \Psi = q(n - p - C), \quad (5)$$

where Ψ is electrostatic potential [V], ε is dielectric constant, and C is a doping, $C = N_D^+ - N_A^-$.

Boundary Conditions Boundary conditions for n, p , and Ψ are shown below for the example of Ohmic contact. At the Ohmic contact we assume thermal equilibrium and vanishing space charge which results in

$$n \cdot p - n_i^2 = 0, \quad (6)$$

$$n - p - C = 0. \quad (7)$$

Solving a quadratic equation for n, p we get Dirichlet conditions for n and p on the boundary (Ohmic contact)

$$n_0 = \frac{1}{2} \left(\sqrt{C^2 + 4n_i^2} + C \right), \quad (8)$$

$$p_0 = \frac{1}{2} \left(\sqrt{C^2 + 4n_i^2} - C \right). \quad (9)$$

The boundary potential at an Ohmic contact is the sum of the externally applied potential (voltage) $V_C(t)$ and the so called built-in potential, which is produced by doping

$$\Psi = \Psi_{bi} + V_C(t). \quad (10)$$

The built-in potential is

$$\Psi_{bi} = U_T \ln \left[\frac{C(x) + \sqrt{C^2 + 4n_i^2}}{2n_i} \right], \quad (11)$$

where the intrinsic concentration n_i is: $n_i = \sqrt{n \cdot p}$. (12)

Solution of Governing Equations for Drift-Diffusion Based Model Governing equations (1) to (4), (5) are examined by the finite volume method and solved simultaneously using the Newton technique, to ensure a good convergence. In NanoTCAD, we use a high-performance iterative linear solver (CNSPACK), developed by Fedoseyev [7]. CNSPACK uses a high order preconditioning by incomplete decomposition to ensure the accuracy, stability and convergence of the simulations. The linear algebraic system is solved in CNSPACK using a CGS-type iterative method with

preconditioning by the incomplete decomposition of the matrix. Comparing the CGS and GMRES methods in different tests, it was found that both methods converge well, if a good preconditioner is used. The CGS method needs less memory to store only eight work vectors. To reduce the memory requirements, a compact storage scheme for matrices is used in CNSPACK. It stores only the nonzero matrix entries. The incomplete decomposition (*ID*) used for preconditioning, is constructed as a product of triangular and diagonal matrices, $\mathbf{P} = \mathbf{LDU}$. To avoid diagonal pivot degeneration, the Kershaw diagonal modification is used [8]. If the value of diagonal element becomes small during the construction of preconditioning matrix, i.e. $|a_{ii}| < \alpha = \sqrt{2^{-t} \sigma \mu}$, the diagonal a_{ii} is replaced by α . Here σ and μ are the maximum magnitudes of current row_i and $column_i$ elements, and 2^{-t} is a machine precision (t bits in mantissa, see the proof of eligibility in [8]). For the first order *ID*, the matrix P has the same non-zero entry pattern as the original matrix. For a second order or higher *ID*, matrix P has one or more additional entries near the locations of the non-zero matrix entries, where the original matrix entries are zeros.

A typical dependence of total memory and CPU time for NanoTCAD simulations of 3D devices using unstructured meshes is almost linear function. Compared to linear solver, used in other commercial device simulators, NanoTCAD solver uses dramatically less memory (by more than one order of magnitude), and CPU time is also smaller by one order of magnitude for similar problem size / number of unknown. NanoTCAD simulator can solve a transient 3D radiation multi-branched ion strike problem with 100,000 node unstructured mesh within 512MB memory. It can solve the problem with 3D unstructured mesh for up to 500,000 nodes within 2GB memory. Typical steady state solution for 3D semiconductor device / solar cell takes 5 to 10 Newton iterations to reach the ten order reduction of initial residual. This corresponds to very short computational time of NanoTCAD (typically a couple of minutes or less). Large transient problems, for example, simulation of radiation effects, produces by high-energy ion strike through the electron device (not relevant to the problems, considered in this paper, please see another our paper [6]), may need more times (few days). This efficient linear solver made possible to use adaptive unstructured 3D mesh generation for a transient 3D multi-branched ion strike problem. We use the Lazarenkova-Balandin model for computation of the electron energy spectra of 3D regimented quantum dot superlattice, which has been proposed earlier [4, 5]. The schematic structure of the quantum dot superlattice is shown in Fig. 5. The electron spectrum is analyzed by using one-electron Schrödinger equation:

$$\left[-\frac{\hbar^2}{2} \nabla_r \frac{1}{m^*} \nabla_r + V(\mathbf{r}) \right] \varphi(\mathbf{r}) = E \varphi(\mathbf{r}) \quad (13)$$

Here $\varphi(\mathbf{r})$ is the electron wave function, E is the electron energy, and the confining potential profile $V(\mathbf{r})$ corresponds to an infinite sequence of quantum dots of sizes L_x, L_y, L_z , separated by the barriers of thicknesses H_x, H_y, H_z . The potential $V(\mathbf{r})$ is set to zero in the barrier region while inside the quantum dot it is equal to the band offset in the conduction (or valence) band of the considered material system taken with a negative sign. The solution of the Schrödinger equations can have semi-analytical approximation using the simplified potential model [13]. Fig. 5(b) shows the results of quantum level approximation only, for the efficiency of the PV cell depending of the QDS dimensions, for a particular material.

Coupling of Quantum and Continuum Level Models of Electronic Device Electron and hole mobility represented by μ_n, μ_p respectively in Eq. (3) and (4) are calculated parameters. Mobility depends on the material, device structure for the continuum transport dominated device region, or calculated from quantum or kinetic level problems for the device regions where the continuum model is not valid. Then, this calculated “quantum” or “kinetic” mobility is used in Eq. (3), (4) for the continuum model. Finally, the whole device is simulated with a continuum level model, using the transport coefficient from quantum level, where this is needed only in the device region with dominated quantum transport, (like the quantum dot layers in Fig. 1). For example, for the quantum dot layers in Fig. 1, we calculate the “quantum” mobility in the device region with quantum dominated transport as follows:

$$\mu_q = \sum \mu_i \frac{n_{si}}{n_s} \quad (14)$$

where $n_{si} = \frac{m}{\pi\hbar^2} \int_{E_{si}}^{\infty} f(E) dE$ is the concentration of electrons in sub-band i with the bottom energy E_{si} , $f(E)$ is Fermi

Dirac distribution function, sub-band mobility $\mu_i = \frac{e}{m} \left\langle \frac{1}{\tau_E} \right\rangle^{-1}$, where the brackets mean the average value. The

electron momentum relaxation time (life time) τ_i in the state E of sub-band i , is calculated using the sub-band energy levels from the solution of Eq. (13) and the scattering rates of an electron, see for example [9], p.205. A similar approach has been successfully developed for the incorporation of kinetic effects into the 3D carrier continuum transport model. Previously, in the device region with strong kinetic effects, we solved the 4D Boltzmann transport equation (BTE), (3D geometry, plus 1D energy space), and macroscopic transport coefficient have been calculated from the kinetic probability distribution function. Results have compared well with the ones published in literature, obtained using accurate sophisticated models, like Wigner equations, and experimental data (see details in [3]). Fig. 2 is an example of the quantum-dot model and photovoltaic power conversion efficiency as a function of the quantum dot size.

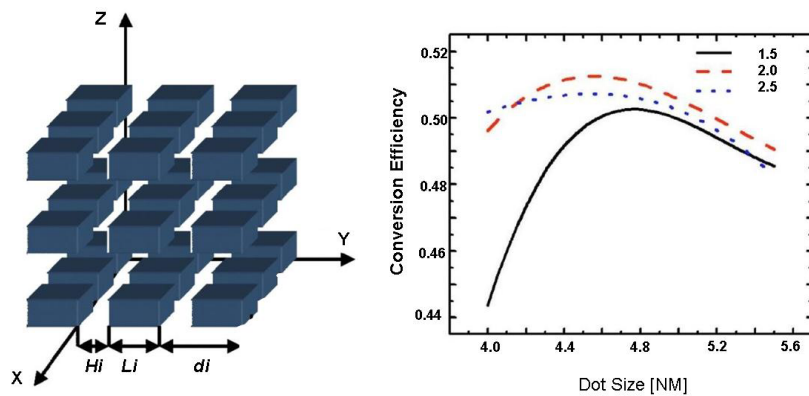


Figure 2. (a) Structure of the QD superlattice - PV cell, L_i , H_i , d_i are dot size, inter-dot separation and QD lattice period in i -direction, $i=x,y,z$. (b) PV energy conversion efficiency as a function of the QD size in $InAs_{0.9}N_{0.1}/GaAs_{0.98}Sb_{0.02}$ superlattice. The results are shown for several inter-dot separations.

Typical I-V curves for photovoltaic device, silicon p-i-n solar cell, calculated with NanoTCAD are shown in Fig. 3(a), and comparison with the experimental data for PV cells developed at RIT are shown in Fig. 3(b).

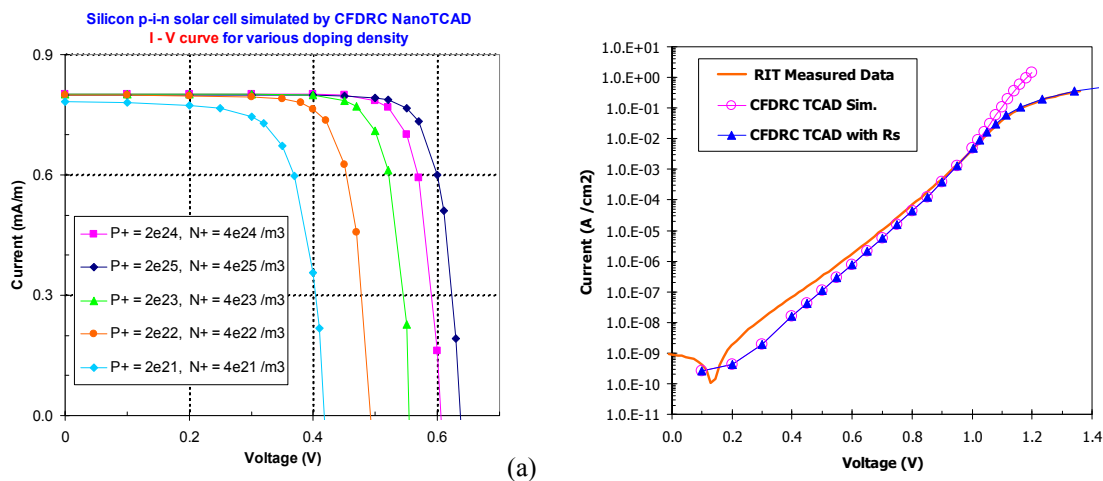


Figure 3. (a) Typical I-V results for solar cell simulation with CFDR NanoTCAD; (b) Comparison of numerical (CFDR) and experimental (RIT) data for PV cell (GaAs cell, $1 \times 1 \text{ cm}^2$).

3. EXPERIMENTAL RADIATION EFFECTS STUDIES OF QD-BASED PV CELLS

Proton irradiation of Solar Cells at UC Davis Crocker Nuclear Laboratory (CNL) To precisely characterize the radiation induced damage in solar cells in a simulated space environment, a number of proton irradiation experiments were conducted on the CFDRC solar cells (six experiments total). Fig. 4 shows experimental setup for irradiation of CFDRC solar cell samples at the CNL isochronous cyclotron, conducted by IPC.

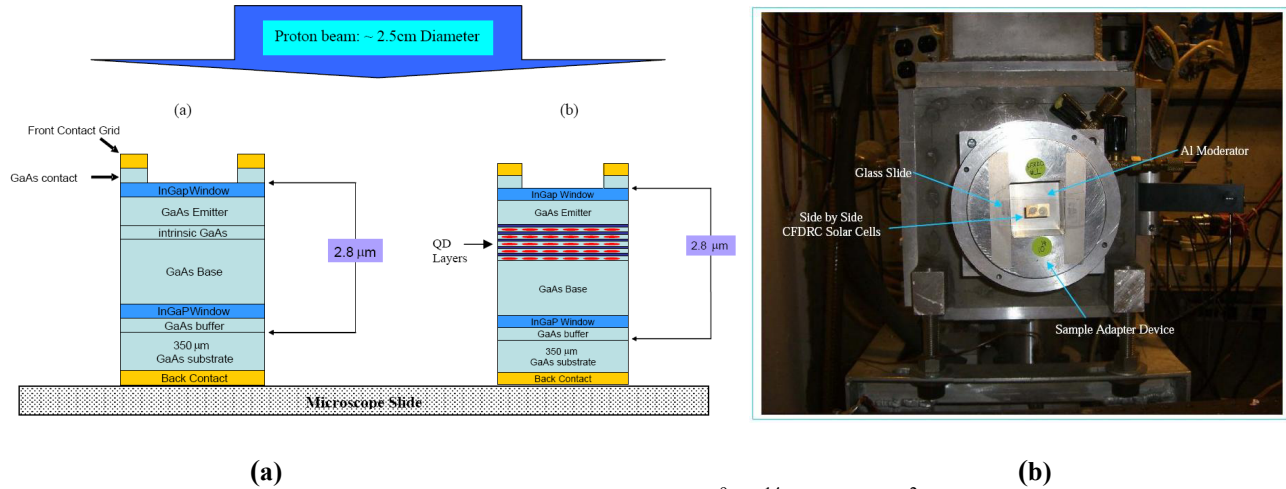


Figure 4. Irradiation of QD PV cell samples at a fluence of $\sim 10^9$ - 10^{14} protons/cm²: (a) Direction of protons aimed at side-by-side (left) regular solar cell and (right) QD-doped cell (figure not to scale). This setup insured identical irradiation conditions for both types of solar cells, to provide a direct comparison of radiation effects in regular and (b) QD-based solar cells at the UC Davis-CNL isochronous cyclotron conducted by IPC. The dosimetry for the irradiated samples is shown in Table 1.

Table 1. Irradiation of PV cell samples at a proton energy of 4.5 ± 0.5 MeV.

CFDRC Samples	Avg Fluence p/cm ²	Avg. Fluence (rounded off)	Avg. Flux (p/cm ² s)E09
13,13b	(Control Device)	N/A	N/A
12,12b	4.445 E09	5 E09	3.4
11,11b	0.998 E10	1 E10	4.5
10,10b	0.997 E11	1 E11	6.7
5,5b	0.990 E12	1 E12	7.4
4,4b	0.992 E13	1 E13	7.6
1,1b	0.991 E14	1 E14	7.8

The average fluence and fluxes specified above were based on Faraday cup measurements. The proton beam profile was approximately 2.5 cm in diameter. In order to achieve the specified lower fluence exposures (10^9 - 10^{11} p/cm²) it was necessary to operate the cyclotron at a lower dose rate (flux) ranging from 3.4 - 6.7×10^9 p/cm²s while for irradiations at higher fluence (10^{12} - 10^{14} p/cm²) the flux ranged from 7.4 to 7.8 p/cm²s. The average beam current for these irradiations ranged between 20 and 45 nA for the lowest and highest applied fluence, respectively.

Arrangement of Samples in Cyclotron Proton Beam Shown in Figure 4(a) is CFDRC Sample No. 1 and 1b mounted side by side on a sample adapter device which is placed in fixed proximity to the proton beam output of the CNL isochronous cyclotron. The back of the glass slide on which the paired samples were affixed is shown spanning a two inch square aperture. The paired samples were centered on the 2.5 cm beam diameter output as shown in Figure 4(b). Using this centering approach, the active regions of the solar cells are facing (and perpendicular) to the proton beam.

Irradiation Conditions All proton irradiations were conducted in air, within a continuous eight hour period, and with the samples at a nominal room temperature of 21 ± 1.2 C. The samples were irradiated while under dimly lighted room conditions and returned to CFDRRC using the CFDRRC provided storage shipping/container immediately after exposure. While the paired chips were briefly exposed to low levels of ambient light, this is not believed to facilitate any significant annealing of proton-irradiation induced effects. The level of light exposure experienced by the chips was minimal since only room-scattered light entering through the back of the glass microscope slide and then perhaps through the substrate would have illuminated the active chip surface areas. The active chip area was facing the beam window which was blocked by the Al-thin film moderator as shown in Figure 4b. Thus, the potential for strong light-induced annealing processes in the chips was minimized.

Comments on the QD impregnated Solar Cell Pre-and Post- Irradiation Results Shown in Fig. 5 is the (SRIM) calculated linear energy transfer (LET) and proton range in GaAs for a proton energy spread of $4.5 \text{ MeV} \pm 0.5 \text{ MeV}$ (indicated by the dotted lines) which represents the uncertainty in the applied proton irradiations. The calculated proton range based on a GaAs density of 5.32 g/cm^3 ($4.4298 \times 10^{22} \text{ atoms/cm}^3$) was far beyond the depth of the detector active area shown in Fig. 1. The calculations show that the protons are fully stopped at $115 \mu\text{m}$ below the cell surface in Fig. 1.

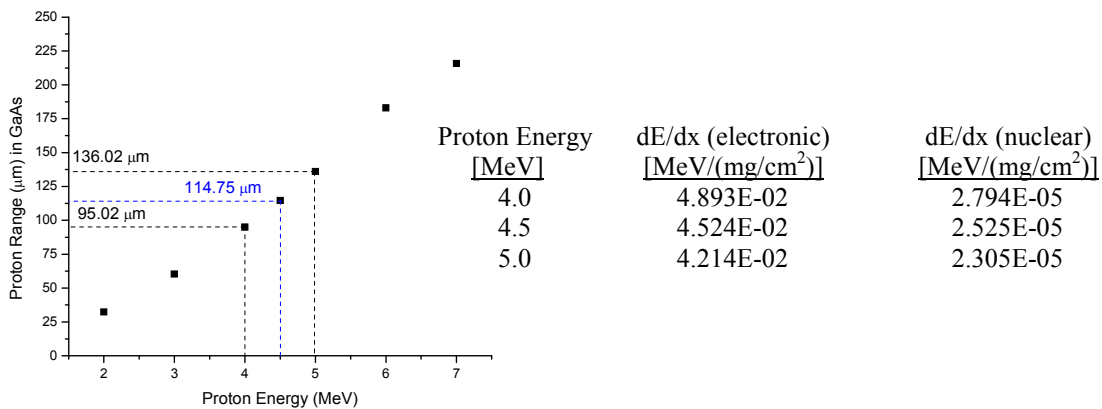


Figure 5. SRIM calculation of proton ranges and LET in GaAs.

It was assumed that the 5x QD detector samples possessed 5x the concentration of QDs as compared to the baseline samples which did not contain QDs. Furthermore, it is assumed that the measurements of wavelength, QE, EQE, etc. were performed under identical conditions for each device and that the lapse in measurement times between the device sample sets was short. The graphics for the sample responses suggest that for the most part there clearly are some subtle proton-induced changes in the QD and non-QD sample responses over the wide range of applied fluence and spectral range(s). This was not unexpected. Based on the proton fluence and average proton energy (4.5 MeV), both the ionization rate and displacement/vacancy rate were calculated as well as the cell structure and materials parameters. The irradiated cells were returned to CFDRRC and then to RIT for post-irradiation testing. Table 2 identifies the cell and proton fluence and flux that each cell received and the calculated TRIM/SRIM results are shown in Fig. 6.

Table 2 Proton fluence and flux for irradiated samples.

Sample	Avg Fluence p/cm ²	Avg. Fluence (rounded off)	Avg. Flux (p/cm ² s)E09
13,13b	(Control Device)	N/A	N/A
12,12b	4.445 E09	5 E09	3.4
11,11b	0.998 E10	1 E10	4.5
10,10b	0.997 E11	1 E11	6.7
5,5b	0.990 E12	1 E12	7.4
4,4b	0.992 E13	1 E13	7.6
1,1b	0.991 E14	1 E14	7.8

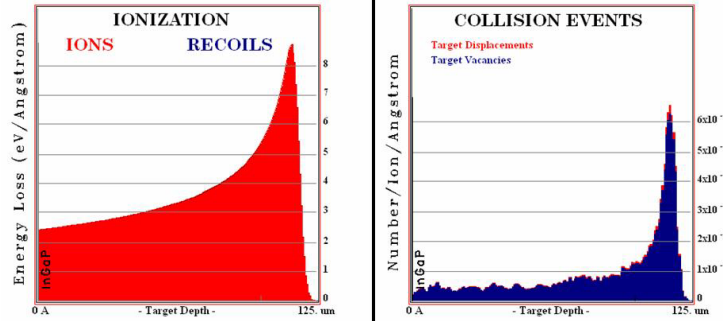


Figure 6. a) Ionization rate for baseline cells b) Displacement/Vacancy Rate for baseline cells

Based on cell structure and material parameters, the non-ionizing energy loss (NIEL) was calculated for our structures for the 4.5 MeV proton irradiations. As seen below, the NIEL is nearly constant in the active region of the cell (first 2.7 μm below the surface). The average NIEL value for 4.5 MeV protons was $2 \times 10^{-2} \text{ MeV} \cdot \text{cm}^2/\text{g}$.

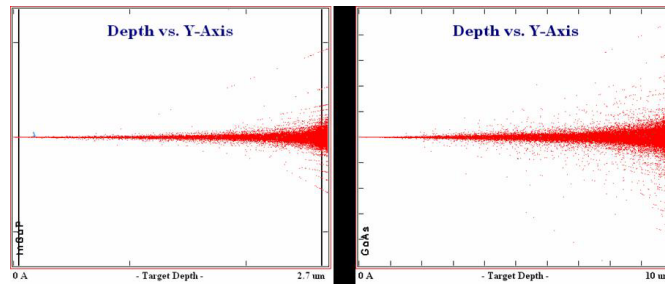


Figure 7. NIEL as a function of depth for our structures

In order to compare results to our previous alpha particle radiation study, proton fluence was converted to displacement damage dose (D_d). Shown below in Figure 8 are one sun AM0 light JV curves for the QD enhanced cells. The displacement damage dose represents the total non-ionizing dose delivered to the material. We degrade the fill factor

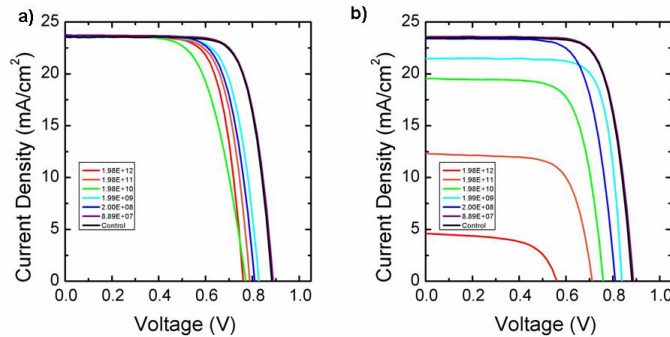


Figure 8. a) One sun AM0 JV curves for all pre-radiation QD cells. b) Post-radiation JV curves for QD cells.

(series resistance) to the extent seen in the baseline devices. Above $2 \times 10^9 \text{ MeV/g}$, QD cell degradation was also more rapid, evidenced by reduction in both J_{SC} (short circuit current density) and V_{OC} (open circuit voltage). However, as will be seen, the rate of degradation in V_{OC} for the QD cell was less as shown in Fig. 9. Both the baseline and QD cell show the same degradation in short circuit current. However, while the actual V_{oc} values for the QD cell were slightly less than the baseline, the relative degradation under high proton flux is less. The QD cell V_{OC} shows improved resistance to proton radiation. In order to investigate further the QD cell radiation tolerance, spectral response was measured for both pre- and post- irradiation baseline and QD cells. Fig. 10 shows that at 810 nm the external quantum efficiency (EQE) is dominated by the GaAs cell.

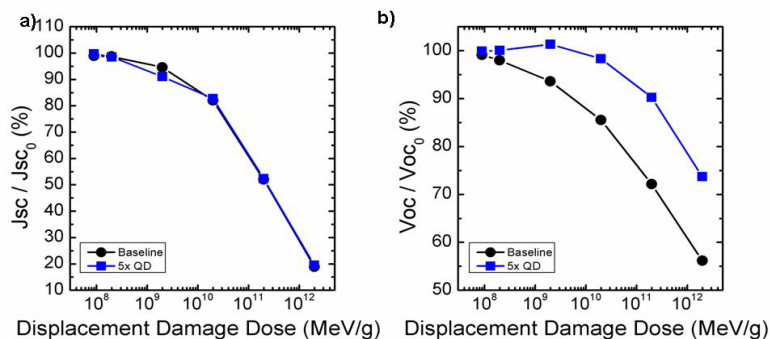


Figure 9. Relative degradation in (a) of JSC and in (b) of Voc as a function of displacement damage dose.

Both QD and baseline devices degrade equally. However, at 910 nm and 1010 nm the GaAs cell has almost no response (photons below the GaAs bandgap), while the QD cell is able to absorb these photons due to the QD bandgap engineering. At these wavelengths, the spectral response of the QDs versus proton dose is approximately constant even under high proton flux

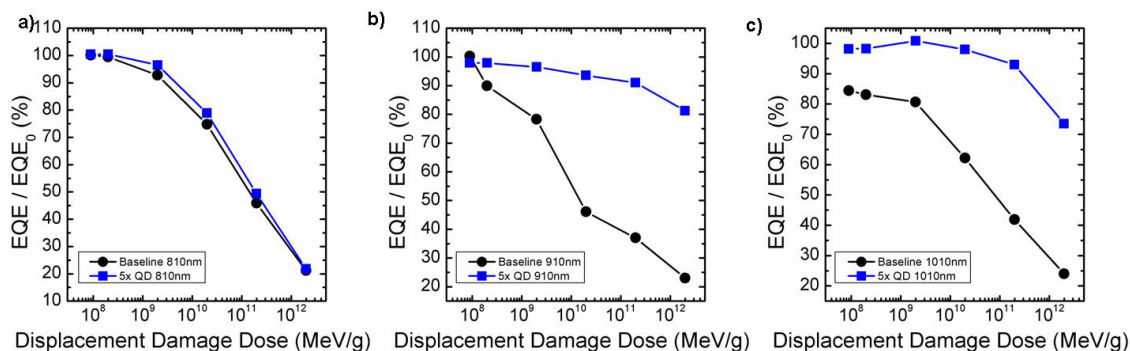


Figure 10. Relative EQE versus D_d at: a) 810 nm, b) 910 nm and c) 1010nm.

Comparison of proton to alpha particle irradiation

The effect of proton irradiation on the performance of QD

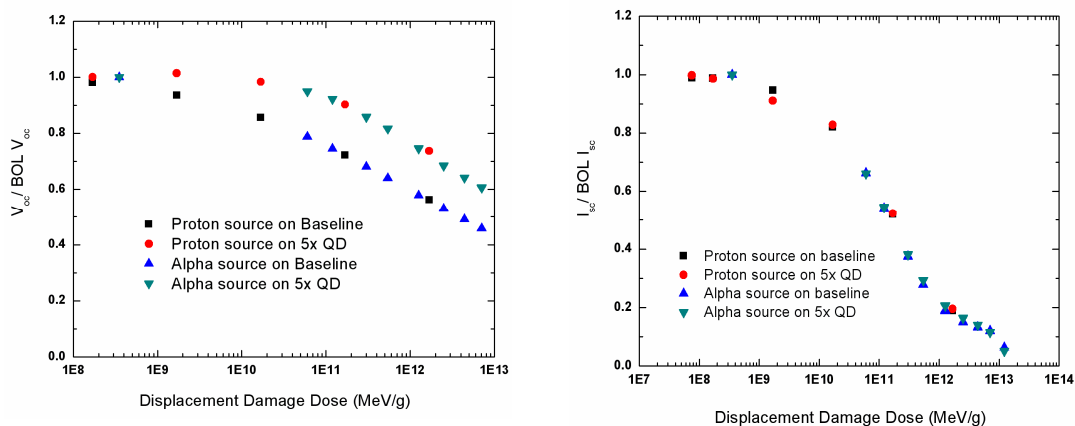


Figure 11. Comparison of proton and alpha particle induced degradation in 5x QD and baseline devices.

solar cells were compared to those observed under irradiation from an isotropic alpha particle radioisotope source on comparable devices [10]. The alpha particle irradiation measurements were conducted on the same device at incremental levels of alpha particle fluence. To normalize the effects of the alpha particle irradiation with that observed

under proton irradiation, the normalized Voc and Isc were plotted with respect to displacement damage dose. Fig. 11(a) depicts the variation in Voc of the QD devices under proton (red circle) and alpha-particle (green triangles) irradiation in reference to their corresponding baseline devices (black square and blue triangle), respectively. The Voc in the 5x QD devices is much more resilient to displacement damage and results in a 10x reduction in the rate of Voc degradation. The primary radiation-induced damage modes leading to a reduced Voc are defects within the depletion region (increased ideality parameter) and increased dark current. It is evident that the QD arrays and the GaP strain compensation layers within the 5x QD cells are mitigating these effects. As expected, a good correlation is observed in the proton and alpha-particle data which validates this dramatic difference observed in the 5x QD and baseline devices. Unlike the Voc, the Isc in all devices has nearly the same response over nearly 5 orders of magnitude of displacement damage dose. The formation of defects within the emitter and base, and to some lesser within the depletion region, leads to a reduction in carrier mobility. As a result, it is expected that all of these cells will have similar Isc variation as shown in Fig. 11(b). Our modeling effort contributes to understanding and explaining this phenomena, and will be utilized in the future for improving the radiation hardness of space solar cells.

4. CONCLUSIONS

We have outlined issues and problems encountered in the development of the quantum-dot based solar cells and comprehensive software tools for simulation and optimization of the nanostructure-based photovoltaic materials. Some experimental results used for the model validation have been reviewed. The novel modeling and simulation tools for the quantum-dot-based nanostructures will help to better understand and predict the behavior of the nano-devices and novel materials in space environment. The irradiation of PV cells and the analysis of results appears consistent and supportive the premise that QDs can play a role in radiation hardening GaAs-based detectors. While the passive irradiations conducted during this study are very informative, in situ (real time-dynamic) proton/electron irradiations would be far more informative for determining the operate-through responses of the devices during the irradiation-degradation process. It is not unreasonable to assume that the post-irradiation changes measured for the irradiated CFDR devices were somewhat diminished compared to real-time responses that might be measured during in situ irradiations. The modeling combined with situ testing can be used to design and further improve space radiation hardened solar cells.

Acknowledgement : This work has been supported by AFOSR under Contract No. FA9550-07-C-0059 and by NASA under Contract No. NNC07CA20C.

REFERENCES

1. Shao Q., Balandin A.A., Fedoseyev A.I. and Turowski M., "Intermediate-band solar cells based on quantum dot supercrystals," *App. Phys. Lett.* 91,163503, (2007).
2. Turowski M., Raman A., and Schrimpf R., "Non-Uniform Total-Dose-Induced Charge Distribution in Shallow-Trench Isolation Oxides", *IEEE Trans. on Nuclear Science*, vol. 51, 3166 (2004).
3. Fedoseyev A.I., Turowski M., and Wartak M.S.: "Kinetic and Quantum Models for Nanoelectronic and Optoelectronic Device Simulation", *J. Nanoelectr. Optoelectr.*, 2, 234–256, (2007).
4. Lazarenkova O.L. and Balandin A.A., "Electron and photon energy spectra in a three-dimensional regimented quantum dot superlattice", *Phys. Rev. B* 66, 245319 (2002)
5. Balandin A.A., Lazarenkova O.L., "Miniband formation in a quantum dot crystal", *J.App.Phys.*, 89, 5505 (2001).
6. Fedoseyev A. I., Turowski M., Raman A., Alles M.L., and Weller R.A., "Multiscale Numerical Models for Simulation of Radiation Events in Semiconductor Devices", Bubak et al (Eds), *ICCS 2008, Part II, LNCS 5102*, pp. 281-290, 2008.
7. Fedoseyev A.I., Bessonov O.A., Iterative solution for large linear systems for unstructured meshes with preconditioning by high order incomplete decomposition, *Comput. Fluid Dynamics Journal*, 10, 296-304 (2001).
8. Kershaw D.S., The incomplete Cholesky-conjugate gradient method for the iterative solution of systems of linear equations. *J. Comput. Phys.* 2, 43 (1978).
9. Landau L. D., Lifshitz E. M. and Pitaevskii L. P.: *Statistical Physics, Science*, p387 (1980).
10. C. D. Cress, B. J. Landi, and R. P. Raffaele, *Trans. Nucl. Sci.* To Appear, 4-08 (2008).